ELSEVIER

Thermochimica Acta 286 (1996) 139–159

thermochimica acta

Enthalpy estimation of the nonequilibrium state in as-melt spun Al–Si and Al–Mn alloys and crystal growth as a nonequilibrium crystallization during rapid unidirectional solidification

Yibin Zhang

Technical Research Institute, HITACHI ZOSEN Corporation, 2-11, Funamachi 2-chome, Taisho-ku, Osaka 551, Japan

Received 24 August 1995; accepted 20 February 1996

Abstract

Rapid solidification as an irreversible process involves an excess enthalpy change, ΔH_{ex}, which is dissipated and stored at the solid–liquid interface, and implies an unreleased part of the latent heat of fusion; this ΔH_{ex} is not negligible on modeling the moving of the solid–liquid interface. In the present paper, the values of ΔH_0^{ne}, the enthalpy difference between rapidly solidified and annealed alloy, were estimated using a DSC measurement method in as-melt spun Al-Si and Al–Mn alloys. The value of ΔH_0^{ne} was related to the excess enthalpy change, ΔH_{ex}. Taking this "thermal engine effect" and the interface kinetic attachment into account, a conceptual model of a "moving boundary problem (MBP)" was formulated to describe the crystal growth during rapid unidirectional solidification. The author attempts to emphasize that this modeling scheme differs from classical MBP, the so-called "Stenfen Problem" in the mathematical formulation and physical contents, due to consideration of the "thermal engine effect".

Keywords: Crystal growth; Moving boundary problem; Rapid solidification; Release of latent heat; Solid–liquid interface

---

1. Introduction

Rapid solidification has been developed for producing nonequilibrium materials with refined structures and excellent mechanical properties using, for example, melt spinning and atomization equipment, and has also been concerned with welding technologies of metals, e.g. using laser beam, electron beam and arc surface melting. It

PII: S0040-6031(96)02931-0

generally requires using high cooling rates or large undercoolings to produce high rates of moving for the solid–liquid interface, so that it results in constrained formations of nonequilibrium structures and nonequilibrium phases. It usually yields crystalline and quasicrystalline products, but it is difficult to obtain a noncrystalline product for most aluminum alloys because the formation of a metallic glass requires extremely high critical cooling rates for aluminum alloys.

Several reports [1–5] have described the microstructural aspects of rapidly solidified aluminum alloys. These have revealed that a sharply evolving microstructure from fine to coarse (or from coarse to fine) formed in a limited scope corresponds with a rapid growth sequence. Moreover, growth morphologies consisting of fine dendrites, a cellular array, banded structure, coupled eutectic and complete solute trapping, are all present in a limited range of about 0.05–1 mm for melt-spun ribbon, and for a laser melting trail in even less than 100 μm. A quantitative relationship between the microstructural morphologies and the advancing velocities of the interface for the crystal growth in several aluminum alloys has been established using a laser melting experiment carried out by Kurz and coworkers [6–9]. They also recognized the evolutionary formation of the banded structure in a transitional region between the cellular and solute-trapping growth. A linear stability theory [10] was introduced to analyze high-speed growth morphologies of rapid unidirectional solidification under an assumption of a dilute binary alloy, in particular, to describe the morphological instability of the advancing interface in terms of the equilibrium and nonequilibrium segregation coefficients of the solute, and to interpret the banding phenomena. Thermodynamic and kinetic analyses for the solute trapping and interface moving [11–13] provided a complicated expression for ΔG, the Gibbs free energy change with respect to the segregation coefficient; this ΔG is not only a thermodynamic driving force for crystallization phase transformation but also a control factor in the kinetics of the moving interface [13]. At the crystal–melt interface, this ΔG actually varies with the microstructural evolution.

It is very important to model the evolutionary formation of the nonequilibrium structures and the phases during rapid solidification, and to predict the solidification conditions of undercooling molten material at the moving front of crystal growth, such as the undercooling temperature and the temperature gradient. In several reports [14–17], the modeling and prediction were approached as a thermal transfer problem governed by long-range transport of molten material towards the external cooling substrate in one dimension. In these approaches, however, the heat source term, indicating a release of solidification latent heat, was treated as the complete liberation of the latent heat of fusion at the interface. These treatments lost the out-of- equilibrium aspect of the enthalpy change. The latent heat evolved in rapid solidification has still not been determined exactly, and it is very difficult to immediately determine the latent heat actually released during rapid solidification. In previous papers [18–20], the author and co-workers proposed a calorimetric evaluation method using differential scanning calorimetry (DSC) measurements to estimate the enthalpy difference ΔH_0^{ne} which exists between as-melt spun ribbons and the fully annealed ribbons, and established the values of ΔH_0^{ne} for several as-melt spun aluminum alloys using this method. It is important to note that this value of ΔH_0^{ne}, as an enthalpy change, implies a non-released part of the latent heat of fusion, and the appearance of the "ΔH_0^{ne} value" is in contradiction with those "complete liberation" approaches of the latent heat of fusion. The non-released part of the latent heat of fusion is not negligible as compared with the completely released part, and this incomplete release effect of the latent heat of fusion, called the "thermal engine effect" in this paper, must be considered in modeling the crystal growth in a rapid solidification process.

The objective of this paper is to formulate a moving interface model for describing the crystal growth as a nonequilibrium phase transformation during rapid unidirectional solidification. This model will approach the crystal growth with microstructural development as a "moving boundary problem (MBP)" including the incomplete release effect of the latent heat of fusion and the kinetic attachment of pulling the interface. The author attempts to use this conceptual model, outlined by initial and boundary conditions that are as simple as possible, to characterize the "thermal engine effect" as the aspect of the enthalpy change during rapid solidification. The present work involved the following. First, we reexamined the evaluation method for ΔH_0^{ne} and the results of the ΔH_0^{ne} value estimated in as-melt spun Al–Si and Al–Mn alloys, and then associated this enthalpy difference, ΔH_0^{ne}, with an excess enthalpy change, ΔH_{ex}, induced by rapid solidification. Then, taking the "thermal engine effect" and the kinetic attachment condition into account, we regulated the crystal–melt interface for crystal growth in order better to reflect the enthalpy change feature of the interface during rapid solidification, which is a nonequilibrium crystallization. Moreover, a conceptual model of moving a crystal–melt interface on the basis of the classical MBP scheme, containing a set of governing equations with initial, boundary, and joint conditions, and an interface kinetic attachment, was formulated to describe the crystal growth in terms of the temperature distribution in the crystal and melt regions, the interface position, and the evolution of the crystallization temperature of the interface. Finally, an attempt briefly to explain the formation mechanism of the banded structure as a "self-excited" oscillatory instability of a high-speed moving interface in this MBP modeling framework was made.

2. Melt-spinning of Al–Si and Al–Mn alloys and the calorimetric evaluation method of the nonequilibrium state

2.1. Sample preparations

The Al–Si and Al–Mn alloys used were prepared in alumina crucibles by melting 99.993 wt% pure aluminum, 99.99 wt% pure silicon and 99.99 wt% pure manganese. The compositions of these binary alloys are tabulated in Table 1. Using a melt-spinning device, shown schematically in Fig. 1, the molten alloys at temperatures higher than 1100 K were squirted with argon gas of 80 kPa pressure on a copper roller, 153 mm in diameter. The roller was rotated at a surface velocity of 17 m s^{-1} for Al–1.66 and –2.56 at %Mn alloys, 36 m s^{-1} for Al–3.95, –5.37 and –6.98 at%Mn and Al–Si alloys. The continuous ribbons obtained had a sectional shape of 3–4 mm in width and 45–80 μm in thickness. This melt-spinning method has been considered to produce a cooling rate

Table 1
Chemical compositions of Al-Si and Al-Mn alloys used in the present paper

Alloys	Composition in at% (wt%)
Al-6.74Si	6.74(7.00) Si
Al-8.48Si	8.48(8.80) Si
Al-11.97Si	11.97(12.40) Si
Al-1.66 Mn	1.66(3.32) Mn
Al-2.56 Mn	2.56(5.07) Mn
Al-3.95 Mn	3.95(7.73) Mn
Al-5.37 Mn	5.37(10.50) Mn
Al-6.98 Mn	6.98(13.26) Mn

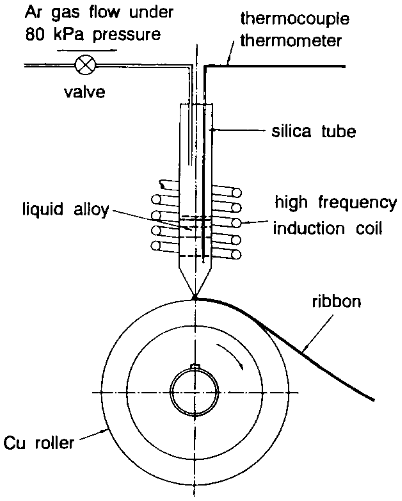

Fig. 1. Schematic diagram of the melt-spinning device used in the present work.

of 10^5-10^6 K s^{-1} for ribbons 30 μm thick [21]. After the ribbons were produced, phases present in the ribbons were identified by X-ray diffraction spectra and selected area diffractions (SAD); the microstructures of these ribbons were detected by an optical microscope, scanning electron microscope (SEM) and transmission electron microscope (TEM).

2.2. Estimation method of the enthalpy difference ΔH_0^{ne}

In order to deduce an estimation method for the enthalpy difference, ΔH_0^{ne}, we first, consider two thermodynamic processes illustrated in Fig. 2. Process 1 involves continuous heating of fully annealed alloys in the equilibrium state from room temperature T_a to a temperature T_b, and then from T_b to the melting point T_m; the enthalpy changes

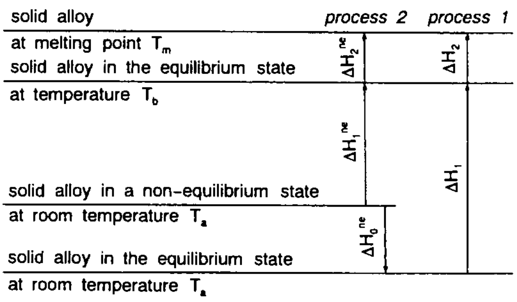

Fig. 2. Schematic illustration of the enthalpy changes during continuous heating of solid alloy in an equilibrium state (Process 1) and in a nonequilibrium state (Process 2).

corresponding to the above-mentioned temperature range are ΔH_1 and ΔH_2 in this reversible process. Process 2 involves continuous heating of an as-melt spun alloy in a nonequilibrium state from room temperature T_a to temperature T_b, and then from T_b to the melting point T_m, the corresponding enthalpy changes being ΔH_1^{ne} and ΔH_2^{ne} in this irreversible process, respectively. ΔH_0^{ne} is given by

$$-\Delta H_0^{ne}+\Delta H_1^{ne}+\Delta H_2^{ne}=\Delta H_1+\Delta H_2 \tag{1}$$

Assuming that $\Delta H_0^{ne}=\Delta H_2$ when the temperature T_b approaches sufficiently close to the melting point T_m, Eq. (2) follows from Eq. (1)

$$\Delta H_0^{ne}=\Delta H_1^{ne}-\Delta H_1 \tag{2}$$

Thus, ΔH_0^{ne} can be approximately evaluated from the difference between the two enthalpy changes, ΔH_1^{ne} and ΔH_1. The following thermodynamic relationship (∂H is the enthalpy change and DQ is the thermal increment)

$$\left(\frac{\partial H}{\partial T}\right)_p=\left(\frac{DQ}{\mathrm{d}T}\right)_p \tag{3}$$

is available for the isobaric process; therefore, it is known that ΔH_1^{ne} and ΔH_1 can be measured by means of calorimetry. In order to obtain ΔH_1^{ne} and ΔH_1, two DSC runs must be performed. In the first DSC run, the DSC curve, $D^{ne}(T)$ of as-melt spun ribbon in a nonequilibrium state should be measured up to T_b. After Mraw [22], $D^{ne}(T)$ can be expressed by

$$D^{ne}(T)=\frac{DQ_s^{ne}}{\mathrm{d}\tau}-\frac{DQ_r}{\mathrm{d}\tau} \tag{4}$$

where $DQ_s^{ne}/\mathrm{d}\tau$ is the heat flow from the heater to the sample, and $DQ_r/\mathrm{d}\tau$ is the heat flow from the heater to the reference in the DSC apparatus. Associating Eq. (3) with Eq. (4), ΔH_1^{ne} can be written in a differential form as

$$\frac{\mathrm{d}(\Delta H_1^{ne})}{\mathrm{d}T}=\frac{\mathrm{d}\tau}{\mathrm{d}T}\left[D^{ne}(T)+\frac{DQ_r}{\mathrm{d}\tau}\right] \tag{5}$$

After the first run the sample should be annealed sufficiently in the DSC apparatus and slowly cooled to room temperature. Thus, the sample can be considered to be in the equilibrium state. The second DSC run starts and the DSC curve, $D^{e}(T)$, should be measured. Evidently, ΔH_1 can also be expressed in the equation

$$\frac{d(\Delta H_1)}{dT} = \frac{d\tau}{dT}\left[D^{e}(T) + \frac{DQ_r}{d\tau}\right] \tag{6}$$

Combining Eqs. (5) and (6)

$$\frac{d(\Delta H_1^{ne}}{dT} - \frac{d(\Delta H_1)}{dT} = \frac{d\tau}{dT}[D^{ne}(T) - D^{e}(T)] \tag{7}$$

Hence, we can obtain Eq. (8) by differentiation of Eq. (2)

$$\frac{d(\Delta H_0^{ne})}{dT} = \left(\frac{1}{\beta}\right)[D^{ne}(T) - D^{e}(T)] \quad (\mathrm{J\,mol^{-1}\,K^{-1}}) \tag{8}$$

where $\beta = dT/d\tau$ is the heating rate of the DSC measurement. The value of ΔH_0^{ne} can be estimated by integration of the $d(\Delta H_0^{ne})/dT - T$ curve

$$\Delta H_0^{ne} = \int_{T_a}^{T_b} \left(\frac{1}{\beta}\right)[D^{ne}(T) - D^{e}(T)]\,dT \quad (\mathrm{J\,mol^{-1}}) \tag{9}$$

We refer to the curve represented by Eq. (8) as a $d(\Delta H_0^{ne})/dT - T$ curve. The peaks on the $d(\Delta H_0^{ne})/dT - T$ curves imply intensive changes in the enthalpy induced by phase transformations in as-melt spun ribbons during heating. Undoubtedly, this enthalpy change, ΔH_0^{ne}, can be estimated from the area integration of the exothermic peaks on the $d(\Delta H_0^{ne})/dT - T$ curve.

2.3. *Performance of DSC measurements*

The values of the enthalpy difference, ΔH_0^{ne}, were evaluated approximately from the above-mentioned DSC measurements, which were carried out at the heating rate of 0.2 K s^{-1} from T_a, 310 K, to T_b, 800 K, for Al–Si alloys and 860 K for Al–Mn alloys in a Rigaku (Rigaku-Denki Co. Ltd., Tokyo, Japan) PTC-10 type apparatus. The instrumental constant was determined by measuring the latent heats of fusion of pure tin, zinc and lead. As-melt spun ribbons of 37–42 mg weight and pure aluminum (99.993 wt%) (reference material) 40 mg in weight were individually packed in aluminum pans for the DSC measurements. Because the eutectic temperature is 850 K for Al–Si alloys and 931 K for Al–Mn alloys, respectively, the temperatures T_b of 800 and 860 K are high enough to reach the equilibrium state expected from the Al–Si and Al–Mn phase diagrams. In fact, no meaningful difference between the X-ray diffraction patterns obtained from the samples after the first and second DSC runs was detected.

3. Calorimetric evaluation results in Al–Si and Al–Mn alloys

3.1. Al–Si alloys

It is obvious from the X-ray diffraction spectra that the melt spinning produced supersaturated α-Al phase in Al–6.74, –8.48 and –11.97 at%Si alloys, and the appearance of a two-zone structure was observed by optical microscope. The $d(\Delta H_0^{ne})/dT - T$ curves of the Al–Si alloys are shown in Fig. 3. A single peak appears in the temperature range 400–600 K for Al–6.74 at%Si alloy, which is caused by the precipitation of silicon phase from the supersaturated α-Al phase. For Al–8.48 and –11.97 at%Si alloys, peaks with two shoulders appear in the temperature range 370–590 K, which is different from the result reported by Apaydin and Smith [23], who indicated that the DSC curve (heating rate 20 K min^{-1}) of as-melt spun Al–12 wt%Si (11.58 at%Si) alloy showed the presence of a shoulder near the main peak. The values of ΔH_0^{ne} and $\Delta H_0^{ne'}$ versus silicon content are shown in Fig. 4. The values of ΔH_0^{ne} can be estimated to be −1.90, −4.45, and −4.59 kJ mol^{-1} for Al–6.74, –8.48 and –11.97 at%Si alloys, respectively. The

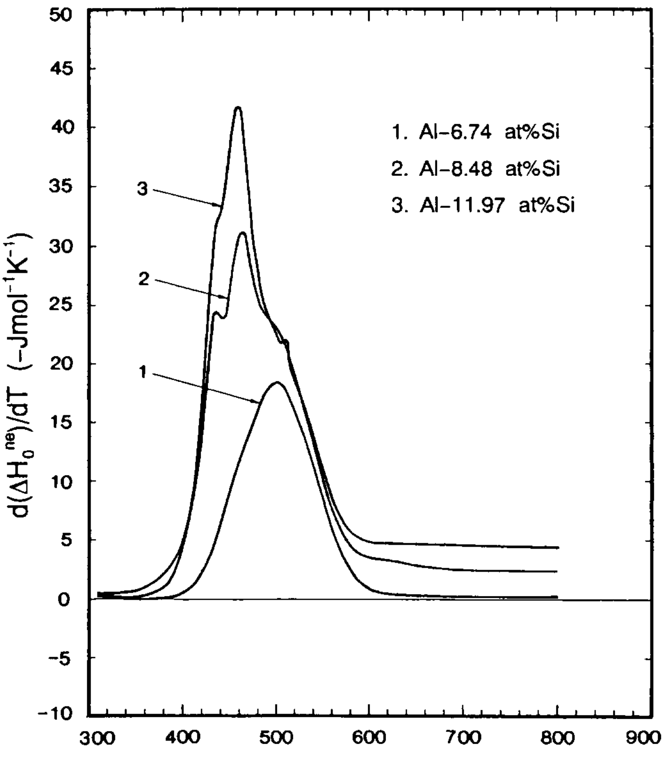

Fig. 3. The $d(\Delta H_0^{ne})/dT - T$ curves at the heating rate of 0.2 K s^{-1} for as-melt spun Al–Si alloys.

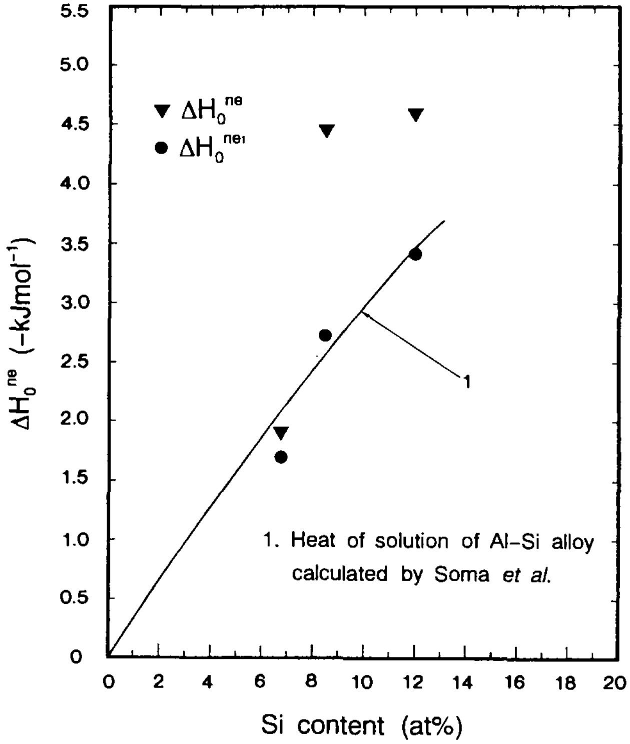

Fig. 4. The enthalpy differences ΔH_0^{ne} and enthalpy changes of Si-phase precipitation $\Delta H_0^{ne\prime}$ versus Si content in as-melt spun Al–Si alloys. The solid line "1" shows the heat of solution of the Al–Si alloy system.

values of $\Delta H_0^{ne\prime}$, -1.70, -2.72 and -3.41 kJ mol^{-1}, increase with silicon content and are in good agreement with the heat of solution calculated by Soma et al. [24] using the microscopic electronic theory based on pseudopotentials and the virtual crystal approximation. Thus, $\Delta H_0^{ne\prime}$ can be attributed to the precipitation of silicon atoms from a supersaturated α-Al phase, or to an essential energy for forming the supersaturated α-Al phase. The values of $\Delta H_0^{ne} - \Delta H_0^{ne\prime}$, -0.20, -1.73 and -1.18 kJ mol^{-1}, for as-melt spun Al–6.73, –8.48 and –11.97 at%Si alloys, may be ascribed to an extremely refined microstructure, sustained by high energies of grain boundaries and substructures. Because the value of ΔH_0^{ne} established by the DSC measurement contains contributions from every part of the as-melt spun ribbon, the evolutionary structure and distribution of the phases formed in transverse section suggest that the distribution function of ΔH_0^{ne} in the ribbons can be related to the distance from the chilled surface. It can be imagined that the value of ΔH_0^{ne} from zone A is larger than from zone B.

3.2. Al–Mn alloys

According to the results of X-ray diffraction and SAD, the ribbons of as-melt spun Al–1.67 and –2.56 at%Mn alloys were solidified as supersaturated α-Al phases, and in ribbons of as-melt spun Al–3.95, –5.37 and –6.98 at%Mn alloys, the icosahedral phase co-existed with supersaturated α-Al phases. Observations by optical microscopy, SEM and TEM revealed that different microstructures and phases are distributed in two-zone regions on both sides in the transverse section of the ribbons [19, 25, 26]. The $d(\Delta H_0^{ne})/dT - T$ curves obtained are illustrated in Fig. 5 for as-melt spun Al–Mn alloys. There is one broad peak corresponding to precipitation of the equilibrium Al_6Mn phase from the supersaturated α-Al phase at about 820 K for Al–1.66 at%Mn alloys [27, 28]. Two peaks, $\mathbf{P}_1$ and $\mathbf{P}_3$, are shown on the $d(\Delta H_0^{ne})/dT - T$ curve for the Al–2.56 at%Mn alloy. Three peaks, $\mathbf{P}_1$, $\mathbf{P}_2$ and $\mathbf{P}_3$ can be seen on each of the curves for Al–3.95, –5.37 and –6.98 at%Mn alloys. The peak $\mathbf{P}_1$ appears at temperatures from about 540 to 560 K, and the peak height is the lowest of the three peaks for each alloy. The peaks $\mathbf{P}_2$ and $\mathbf{P}_3$ become higher and both peak temperatures shift to the lower side with increasing manganese content. According to other reports on phase transformations during continuous heating of melt-spun ribbons of Al–Mn alloys by DSC measurements [27–29], the peak occurring at about 550 K on the DSC curves corresponds to precipitation of the icosahedral phase in the supersaturated α-Al solid

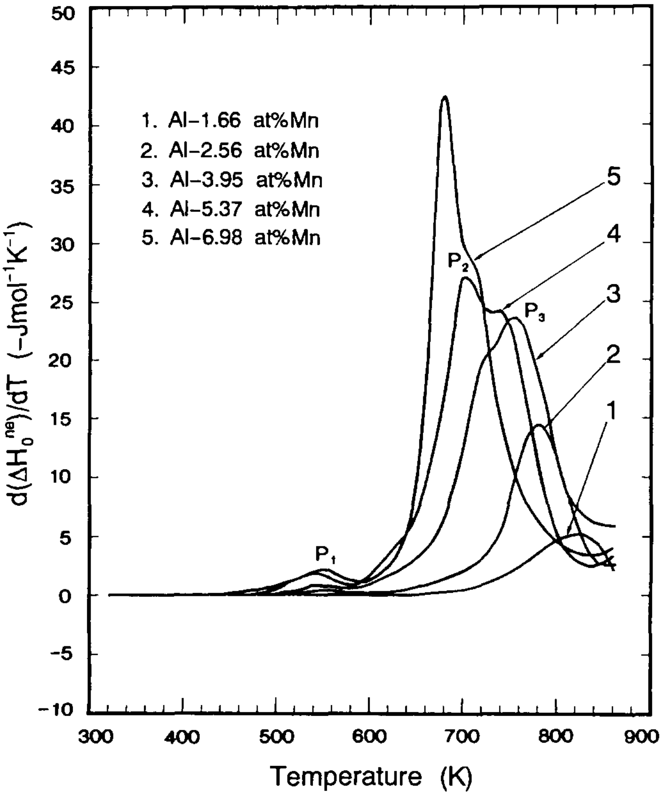

Fig. 5. The $d(\Delta H_0^{ne})/dT - T$ curves at the heating rate of 0.2 K s^{-1} for as-melt spun Al–Mn alloys.

solution. The peaks $\mathbf{P}_2$ and $\mathbf{P}_3$ in the temperature range from 600 to 820 K (depending on manganese content) are attributed to transformation of the icosahedral phase to the equilibrium Al_6Mn phase and precipitations of Al_6Mn and $Al_{12}Mn$ phases from the supersaturated α-Al solid solution, respectively. The peaks $\mathbf{P}_2$ and $\mathbf{P}_3$ shift to higher temperatures and the peak heights are reduced with increasing manganese content. In the present work, peak $\mathbf{P}_1$ at about 500–580 K may be due to the precipitation and growth of networks of the icosahedral phase at the α-Al cell boundaries, which were confirmed by TEM after annealing the ribbons at 490 K for 14.4 ks [19]. The values of ΔH_0^{ne} and $\Delta H_0^{\mathrm{ne'}}$ are plotted against manganese contents in Fig. 6. ΔH_0^{ne} increases with increasing manganese content, and the trend in the ΔH_0^{ne} increments is remarkable in the range from about 2 to 4 at%Mn. The values of ΔH_0^{ne} are -2.82, -3.28 and -3.48 kJ mol^{-1} for Al–3.95, -5.37 and -6.98 at%Mn alloys, respectively. The change with manganese content in the value of $\Delta H_0^{\mathrm{ne'}}$, which corresponds to the energy stored in various kinds of nonequilibrium phases, reveals a remarkable increment with increasing manganese content. The values of $\Delta H_0^{\mathrm{ne}} - \Delta H_0^{\mathrm{ne'}}$ are very small for the Al–1.66 and -2.65 at%Mn alloys. For the Al–3.95, -5.37 and -6.98 at%Mn alloys, they become large and nearly the same.

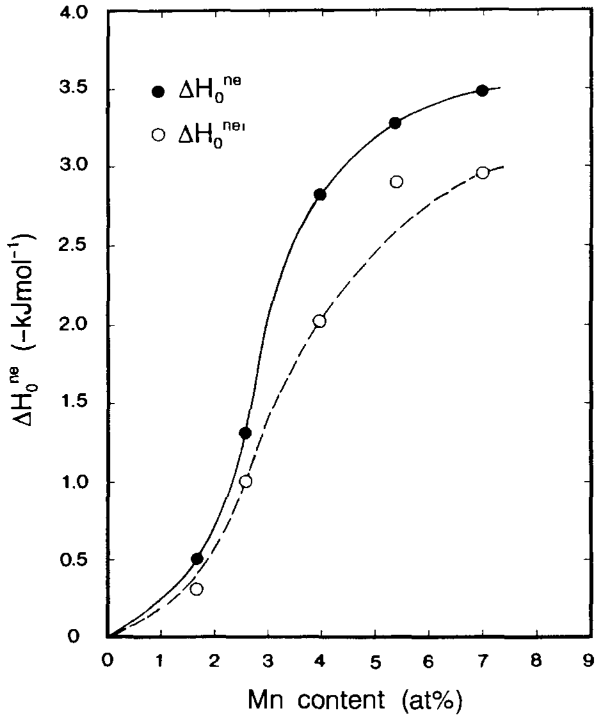

Fig. 6. Changes in the enthalpy differences ΔH_0^{ne} and $\Delta H_0^{\mathrm{ne'}}$ with Mn content for the Al–Mn alloys, which were both calculated from each $\mathrm{d}(\Delta H_0^{\mathrm{ne}})/\mathrm{d}T - T$ curve as shown in Fig. 5.

4. The value of ΔH_0^{ne} and an excess enthalpy change, ΔH_{ex}: the "thermal engine effect"

The enthalpy difference, ΔH_0^{ne}, as thermal energy, is stored in as-melt spun ribbon during rapid solidification, and it conversely implies a dissipated enthalpy in the irreversible phase transformation process. For as-melt spun Al–Si and Al–Mn alloys, because the solute-limited solubilities of silicon and manganese in the α-Al solution phase are relatively small, it can be considered that the value of ΔH_0^{ne} is approximately equal to this dissipated enthalpy change denoted by ΔH_{ex}, which is called the excess enthalpy change induced by a nonequilibrium crystallization phase transformation. It is interesting to compare the enthalpy change $\Delta H(T_{\mathrm{m}})$ involved in the equilibrium crystallization of a eutectic melt at the melting point T_{m}, with an enthalpy change $\Delta H(T)$ involved in a nonequilibrium crystallization of the eutectic melt at a temperature T lower than the melting point T_{m}. Both enthalpy changes, $\Delta H(T_{\mathrm{m}})$ and $\Delta H(T)$, from a liquid temperature T_{l} to room temperature T_{a} should be respectively

$$\Delta H(T_{\mathrm{m}}) = \int_{T_{\mathrm{l}}}^{T_{\mathrm{m}}} C_{p\mathrm{l}} \mathrm{d}T + L_{\mathrm{m}} + \int_{T_{\mathrm{m}}}^{T_{\mathrm{a}}} C_{p\mathrm{c}} \mathrm{d}T \tag{10}$$

and

$$\Delta H(T) = \int_{T_{\mathrm{l}}}^{T} C_{p\mathrm{l}} \mathrm{d}T + L(T) + \int_{T}^{T_{\mathrm{a}}} C_{p\mathrm{c}} \mathrm{d}T \tag{11}$$

where L_{m} is the latent heat of fusion, $L(T)$ is a liberation of solidification latent heat at the temperature T, and $C_{p\mathrm{l}}$ and $C_{p\mathrm{c}}$ are the volume-specific heat capacities of the liquid alloy and solidified crystal, respectively. The excess enthalpy change ΔH_{ex} is expressed by

$$\Delta H_{\mathrm{ex}} = \Delta H(T_{\mathrm{m}}) - \Delta H(T) = \int_{T_{\mathrm{m}}}^{T} (C_{p\mathrm{c}} - C_{p\mathrm{l}}) \mathrm{d}T + L_{\mathrm{m}} - L(T) \tag{12}$$

Neglecting the integration term $(C_{p\mathrm{c}} - C_{p\mathrm{l}})\mathrm{d}T$ on the right-hand side, ΔH_{ex} can be written approximately as

$$\Delta H_{\mathrm{ex}} = L_{\mathrm{m}} - L(T) \tag{13}$$

Therefore, the excess enthalpy change ΔH_{ex}, as a thermal energy, should be considered to be an incomplete release of the latent heat of fusion for a nonequilibrium crystallization process. For the sake of simplicity, we considered the case of a eutectic alloy in the above; however, this "thermal engine effect" is also available for an off-eutectic alloy due to the thermodynamic implication. For an off-eutectic alloy, the crystallization occurs in a temperature range between the liquidus and solidus, and this temperature range shrinks with increasing velocity of crystal growth, and finally becomes a temperature T_0 on forming the complete solute solution. The striking values of ΔH_0^{ne} estimated in the Al–Si and Al–Mn alloys, a large un-released part of the latent heat of fusion as compared with 10.47 kJ mol^{-1}, the latent heat value of fusion of pure aluminum, are not negligible for modeling the crystal growth during rapid solidification.

We now liken a melting and rapid solidification cycle to a Carnot cycle, i.e., in the melting, the absorbent latent heat is L_m, and in the rapid solidification, the released latent heat for the nonequilibrium crystallization is $L(T)$. In this Carnot cycle, the "thermal engine" efficiency η can be introduced and should be written as

$$\eta = \frac{\Delta H_{ex}}{L_m} = \frac{L_m - L(T)}{L_m} \tag{14}$$

This thermal engine efficiency η measures the nonequilibrium departures in the released latent heat of the crystallization reaction. This thermal efficiency η, as a "pure enthalpy efficiency", differs from the Carnot efficiency term, which was related to $\Delta T/T_m$ or $\Delta G/L_m$, and was mentioned previously by Baker and Cahn [30] to explain the undercooling ΔT during the solidification process. It should be restricted by the thermodynamic constraints, and should vary with Gibbs free energy change ΔG for the crystallization, and the crystallization temperature T. If the solute-limited solubility of a binary system is considered sufficiently small, we can classify the solidification reaction of the binary alloy by the order of magnitude of the thermal efficiency η to the following five types, and in this classification, ΔG, η and T should be respectively:

1. Equilibrium crystallization with the latent heat of fusion L_m and no "thermal engine effect", $\Delta G = 0, \eta = 0$ and $T = T_m$, or the temperature T will be in the range of the liquidus and solidus.

2. Solute trapping as a nonequilibrium crystallization with released latent heat $L_m - \Delta H_s$, and a stored thermal energy ΔH_s, which is the heat of complete solution [24]: $\eta = \Delta H_s/L_m$, $\Delta G < 0$, and $T = T_0$. ΔG has been expressed in general by Baker and Cahn [30] as

$$\Delta G = (\mu_A^\alpha - \mu_A^l)(1 - X_B^\alpha) + (\mu_B^\alpha - \mu_B^l)X_B^\alpha \tag{15}$$

where μ_A^α, μ_A^l, μ_B^α, μ_B^l are chemical potentials of elements A and B in solidified α-phase solution and in the liquid, respectively, and X_B^α is the concentration of element B in the α-phase solid. Another expression for ΔG is [31]

$$\frac{\Delta G}{RT} = \frac{(1 - k_v C_l)C_l(k - k_v)}{1 - kC_l} + k_v C_l \ln\left(\frac{k_v}{k}\right) \tag{16}$$

where C_l is the alloy composition, k is the equilibrium segregation coefficient of the solute determined by the equilibrium phase diagram, and k_v is the nonequilibrium segregation coefficient of the solute. When the temperature of the solid–liquid interface is below T_0, a critical temperature below which the phase transformation proceeds with no solute segregation, complete solute trapping occurs with $k_v = 1$ and results in the formation of a supersaturated solid solution [32].

3. Nonequilibrium crystallization (including quasicrystallizations): $T_0 < T < T_m$, $0 < \eta < \Delta H_s/L_m$, $\Delta G < 0$.

4. Nonequilibrium crystallization forming a crystal solution with high density defects: $T < T_0$, $\Delta H_S/L_m < \eta < 1$, $\Delta G < 0$.

5. Nonequilibrium solidification forming amorphous phase without latent heat release: $\eta = 1$, $\Delta G < 0$, $T < T_g$, where T_g is a critical temperature of metallic glass transformation.

In the present paper, the crystal growth indicates the evolutionary formation of a crystal with defects or second-phase crystals, and of quasicrystals for a binary aluminum alloy, which indicates in particular moving the interface which loads a crystal reaction system. In a later section, a conceptual model of the crystal growth including the "thermal engine effect" will be formulated in a set of governing equations of heat transfer. This model also considers the approach of the interface response functions of the Gibbs free energy change ΔG, the thermal efficiency η and the crystallization temperature T_i with respect to the interface position.

5. Modeling the crystal growth including the thermal engine effect: A moving boundary problem

5.1. Regulation of the crystal–melt interface

In order to take the thermal engine effect into account in the crystal growth modeling, it is necessary to regulate the crystal–melt interface for the growth formation of single or multi-phase crystals. Treating the crystal–melt interface, one must consider the mobility, crystallization reaction, thermodynamic constraints, kinetic attachment and local heat balance. Therefore, the definition of the crystal–melt interface must involve the following aspects:

1. The crystal–melt interface indicates a mobile boundary or flat zone within a volumetric element at the front of the growing crystal; it is sandwiched between both crystalline and molten domains but does not belong to both of them. Moving the interface ultimately brings about crystal growth.
2. Inside the interface, equilibrium or nonequilibrium crystallization reaction occur and result in the formation of single or multi-phase crystals. The reaction process includes the nucleation and its growth, governed by solute diffusion; in other words, from the onset of crystal nucleation to when the crystals occupy the whole volume space of the interface, the solute diffusion related to the crystallization reaction occurs only inside the interface.
3. At the interface, the crystallization reaction system is driven by a Gibbs free energy difference, ΔG, between the crystals formed and the molten alloy, and the interface temperature T_i, a characteristic or effective temperature, not only indicates an undercooling temperature caused by external cooling, but also an actual response temperature of the crystallization reaction system. The "interface nonequilibrium" signifies that the Gibbs free energy change ΔG, the thermal efficiency η and the crystallization temperature T_i, deviate systematically from local thermodynamic equilibrium at the interface.
4. Only the interface is a volumetric heat source for generating solidification latent heat, and the virtual generation of solidification latent heat at the interface $L(T_i)$ with respect to the thermal engine efficiency η should be

$$L(T_i) = L_m(1 - \eta) \tag{17}$$

This approach actually deals with the local heat balance condition of the crystal front, where the thermal engine is working, and describes the excess enthalpy change stored at the advancing interface.

5. The moving velocity of the crystal–melt interface V can be related to a thermodynamic driving force ΔG for pulling the interface and the interface temperature, T_i, as the interface kinetic attachment, i.e. in the Aziz equation [13], which is expressed by

$$V = V_c\left[1 - \exp\left(\frac{\Delta G}{R T_i}\right)\right] \tag{18}$$

where V_c is a kinetic rate parameter for crystallization, and R is the gas constant.

Following this, there are three types of crystal–melt interface, classified from the solute segregation and Gibbs free energy difference between the crystallized solid and the melt for an aluminum binary alloy, as illustrated in Fig. 7. these are:

1. The equilibrium crystallization case, $\Delta G = 0$, $\eta = 0$; the molten C_l segregates into two equilibrium crystals with the equilibrium concentrations C_α and C_β. This type of interface results in the structural formation related to a normal casting process.
2. A nonequilibrium crystallization case, $\Delta G < 0$, $0 < \eta < \Delta H/L_m$; the molten C_l segregates into two nonequilibrium crystals with concentrations C'_α and C'_β, which results in the nonequilibrium formation of multi-phase structure, such as supersaturated α-Al phase, icosahedral phase and coupled eutectic phases. This type of the interface implies a "mushy zone", which provide a large area with respect to the structural formation of various morphologies.
3. The solute trapping case, $\Delta G < 0$, $\eta = \Delta H_S/L_m$; the molten C_l solidifies the supersaturated α-Al solution with $C^*_\alpha = C_l$. This type of interface causes mostly a plane-fronted crystal growth.

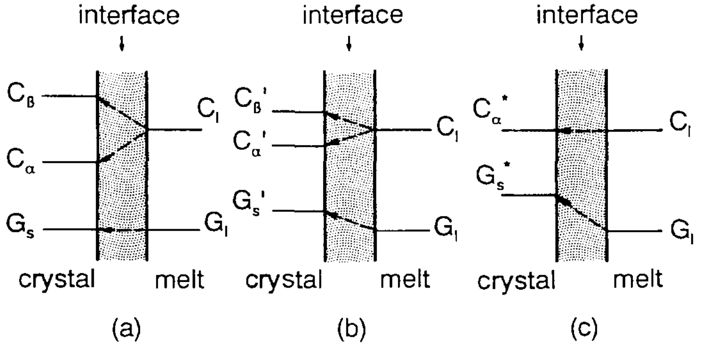

Fig. 7. Three types of crystal–melt interface for the crystallization of a binary aluminum alloy, classified from solute segregation and Gibbs free energy difference between crystallized solid and molten phase.

5.2. Modeling on moving the crystal–melt interface governed by thermal transfer

Consider the crystal growth in an undercooling melt, governed by one-dimensional heat conduction with rapid unidirectional solidification. This crystal growth can be described as follows: a rapidly propagating temperature field is created by strong heat extraction of the cooling substrate, the temperature distribution in the temperature field is decided by long-range diffusion of thermal energy, and the crystal–melt interface advances from the substrate surface towards the semi-infinite melt in order to catch up with the temperature field in the fixed direction. Under the stability assumptions of: (1) no relative moving of liquid and solid conduct media, (2) no disordered heat flow, and (3) the transport direction of the heat flow being perpendicular to the cooling substrate which is a heat sink of absorbing thermal energy, we can approach the crystal growth by using the front-tracking method, i.e., as a "moving boundary problem (MBP)" [31,33].

Fig. 8 schematically shows the semi-infinite sheet along the coordinate x. The crystallization initially occurs as a nonequilibrium reaction on the substrate surface $x = 0$ at a temperature T_{sb}, which is lower than T_m, and develops in the positive direction of the coordinate x, finally finishing as an equilibrium case at T_m. Hence, a decelerated movement of the crystal–melt interface begins from $x = 0$ and progresses in a positive x direction. The interface response function of the crystallization temperature, or the

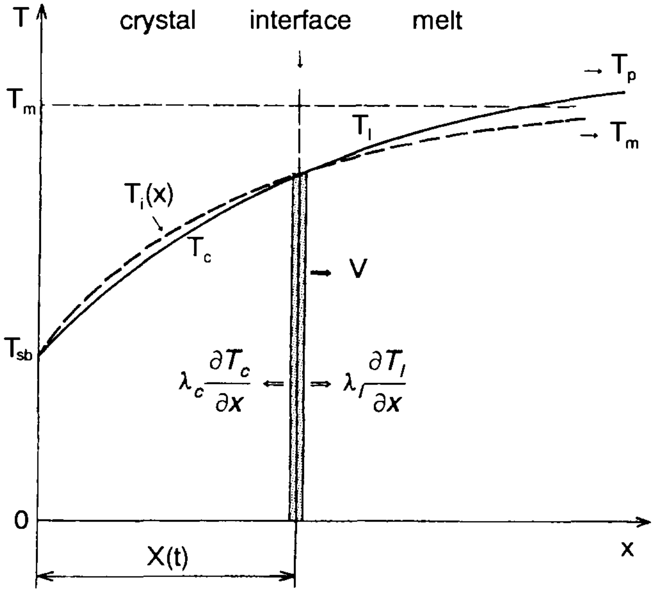

Fig. 8. Schematic drawing of moving crystal–melt interface in a semi-infinite sheet. The molten enthalpy is extracted by a conduct substrate on the left side. "V" indicates the velocity and direction of crystal growth during the rapid unidirectional solidification.

evolution of the interface temperature, is $T_i(x)$, and the position of the interface (center transverse section) at time t is denoted by $x = X(t)$. The temperature field is described by a divided two-temperature distribution $T_c(x, t)$ and $T_l(x, t)$ in the crystalline solid and molten domains respectively. In the crystal solid domain, $0 < x < X(t)$, the one-dimensional equation of heat transfer with constant material properties should be

$$\rho_c C_{pc} \frac{\partial T_c}{\partial t} = \lambda_c \frac{\partial^2 T_c}{\partial x^2} \tag{19}$$

and in the domain $x > X(t)$, the governing equation should be

$$\rho_l C_{pl} \frac{\partial T_l}{\partial t} = \lambda_l \frac{\partial^2 T_l}{\partial x^2} \tag{20}$$

where ρ_c and ρ_l are the mass densities of the solidified crystals and the melt, and λ_c and λ_l are the heat conductivities of the crystalline solid and the melt, respectively. Subject to the fixed boundary and initial conditions:

$$T_c(0, t) = T_{sb} \quad T_c|_{x \to \infty}(x, t) = T_m$$

$$T_c(x, 0) = T_{sb} \quad x = X(0) = 0$$

$$T_l(0, t) = T_{sb} \quad T_l|_{x \to \infty}(x, t) = T_m$$

$$T_l(x, 0) = T_{sb} \quad T_l|_{x \to \infty}(x, 0) = T_p$$

These conditions are as simplified as possible. The continuity of the temperature distribution gives a joint condition at $x = X(t)$, namely

$$T_c(X(t), t) = T_l(X(t), t) = T_i(X(t))$$

This interface temperature $T_i(X(t))$ will be a variable but not a constant one, the melting point T_m. Application of Fourier's law to both sides of the interface gives a heat flux balance condition towards and away from the interface. This heat flow balance, as a joint condition at $x = X(t)$, should involve a virtual generation of the latent heat as defined in Eq. (17). This joint condition of the heat flow should be

$$\lambda_c \frac{\partial T_c}{\partial x} - \lambda_l \frac{\partial T_l}{\partial x} = \rho_c L_m (1 - \eta(X(t))) \tag{21}$$

and in this joint condition of heat flow, the thermal engine effect is taken into account in the heat source term and reflected in the term for the interface response function of the thermal engine efficiency, $\eta(X(t))$. Moreover, following Eq. (18), the interface kinetic attachment at $x = X(t)$ can be written as

$$V(X(t)) = \frac{\mathrm{d}X(t)}{\mathrm{d}t} = V_0 \left[1 - \exp\left(\frac{\Delta G(X(t))}{R T_i(X(t))} \right) \right] \tag{22}$$

where $V(X(t))$ is the momentary speed of displacement of the interface, and $\Delta G(X(t))$ is the interface response function of the Gibbs free energy change. Eqs. (19) and (20) with the boundary, initial, and joint conditions and the interface kinetic attachment constitute a mathematical framework (an MBP modeling) to describe the movement of the interface for crystal growth. The solution of this set of equations aims to obtain the temperature distributions $T_c(x, t)$ and $T_l(x, t)$ in the two domains, the trend of the interface temperature $T_i(x)$ and the interface position $x = X(t)$.

The classical MBP, the well-known "Stenfen problem", was approached by Stenfen and its analytical solution was carried out by Neumann for an equilibrium crystallization case, such as the ice–water transformation. The difference in mathematical formulations between the present MBP model and the classical MBP is as follows: for the present modeling, (1) a variable interface temperature $T_i(x)$ is the temperature joint condition between two domains, whereas in classical MBP it is a constant temperature, T_m; (2) a variable volume heat source of heat generation is the heat flux joint condition between two domains; in classical MBP, it is a constant heat generation, the latent heat of fusion, L_m; and (3) the moving velocity of the interface is also restricted by the kinetic attachment; in classical MBP, this is not a kinetic restriction. Classical MBP is suitable only for equilibrium problems; however, the present conceptual model covers a wider extent of phase transformation process from the equilibrium to nonequilibrium crystallization, and is expected to describe a continuous succession of crystal growth from solute trapping to equilibrium solidification. The present MBP model also maps the trend in Gibbs free energy change ΔG and excess enthalpy change ΔH_{ex} in terms of interface response functions, $\Delta G(X(t))$ and $\eta(X(t))$, which leads to a more complicated formulation of the governing equations, and a more difficult computation for the solution of the governing equations. The solution of the present MBP model is expected to employ a numerical analytical time-stepping method that depends on the establishment of the relationships $\eta(T_i)$ and $\Delta G(T_i)$, which are profoundly related to the solute segregation and morphological evolution. The nonequilibrium thermodynamic and kinetic analysis for the interface, carried out by Boettinger and Aziz [12, 13], seems possibly to provide an analytical expression $\Delta G = f(T_i, k_v)$. However, the relationship between the thermal efficiency η and the interface temperature T_i is pending further discussion on the statistical thermodynamics, and seems to require more sophisticated measurement. It can be predicted that $T_i(x)$ will be a monotonic, stable function, except for $\eta(X(t))$ and $\Delta G(X(t))$ being unstable.

5.3. *Evolutionary crystal growth with banded structure*

The evolutionary crystal growth with the banded structure, which consists of a regular succession of dark and light bands, was observed in rapidly solidified Ag–Cu, Al–Cu and Al–Fe binary alloys [7, 8, 21, 32, 34], and the existence of the bands as "growth rings" in a transitional border between zones A and B was also recognized in as-melt spun Al–Mn–Co alloys and seems to present in as-melt spun Al–Mn alloys [25, 26]. Laser remelting experiments of Al–Fe and Al–Cu alloys have quantitatively confirmed that the banded structure is formed in a transitional region from two-phase crystal growth with dispersoids to crystal growth of α-Al phase solution in the intermediate range of velocities of the order of several tenths of a m s^{-1}, when the solute trapping begins to act [7, 8].

In the regular banded structure of the aluminum alloys, the light band is characterized by columnar grains of supersaturated α-Al solution without any particles, formed by solute trapping, and the dark band is composed of α-Al phase microcells with second-phase dispersoids of the order of several tenths of a nm, formed by segregation crystallization. The formation of the dark band may conform to a model proposed by Cotton and Kaufman [4], i.e., the dispersive nuclei initiate in the liquid alloy, and then the α-Al phase solution rapidly engulfs the dispersoids. Thus, the nucleation of the dispersoids may play an important role in the formation of the bands. In classical nucleation theory, the homogeneous nucleation frequency I_f is given by

$$I_f = N \exp\left(-\frac{\Delta G_A}{k_B T}\right) \tag{23}$$

where the N term is approximately constant, k_B is the Boltzmann constant, ΔG_A is the activation energy for the nucleation, and T is the temperature of the nucleation. The nucleation frequency I_f will reach a larger value at an undercooling temperature which is lower than 0.2 T_m, under which temperature the nucleation must overcome a large activation energy. The alternate arrangement of the dark and light bands suggests an oscillatory fluctuation in Gibbs free energy change, ΔG induced by the critical activation energy for the nucleation. Based on this consideration, an attempt to explain the banding phenomena will be made in the framework of the present MBP modeling.

Fig. 9 shows the evolution of a structure containing the bands, and the interface response functions of the thermal efficiency $\eta(x)$ and the crystallization temperature $T_i(x)$ during the growth formation of this structure, which is actually produced by a continuous progress of three types of interface, as shown in Fig. 7, i.e., from solute trapping on left to equilibrium crystallization on the right. A regular banded structure, as shown schematically in Fig. 9(a), is sandwiched between the α-Al solution region on the left and the $\alpha + \beta$ two-phase region on the right. The banded structure consists of a periodic arrangement of α light bands and $\alpha + \beta$ dark bands, the relative volume fractions of the light and dark bands being approximated from a quantitative result determined by Zimmermann et al. [6]. Fig. 9(b) illustrates the interface response function of the thermal efficiency, $\eta(x)$, which should correspond to an oscillatory curve in the banding region, i.e., which gets to a threshold value η(b) for the light band and a threshold value η(c) for the dark band. The difference between the threshold values η(b) and η(c) indicates a difference in the released latent heat between the light and dark bands, and implies a critical activation energy for dispersoid nucleation in the dark bands. Although it oscillates, to total value of $\eta(x)$ in a pair of coupled light and dark bands should reduce gradually from the threshold value η(b) to the threshold value η(c), as shown by the dashed line. Fig. 9(c) exhibits the interface response function of the temperature $T_i(x)$, which oscillates corresponding to the oscillation of $\eta(x)$ in the banding region. Similarly, the total temperature value in a pair of coupled light and dark bands should gradually change despite $T_i(x)$ oscillations. For Al–2 wt%Fe alloy, the temperature oscillation of the solid–liquid interface to form the banded structure has been calculated by Gremaud et al. [7] to be about 5 K. Therefore, if the heat

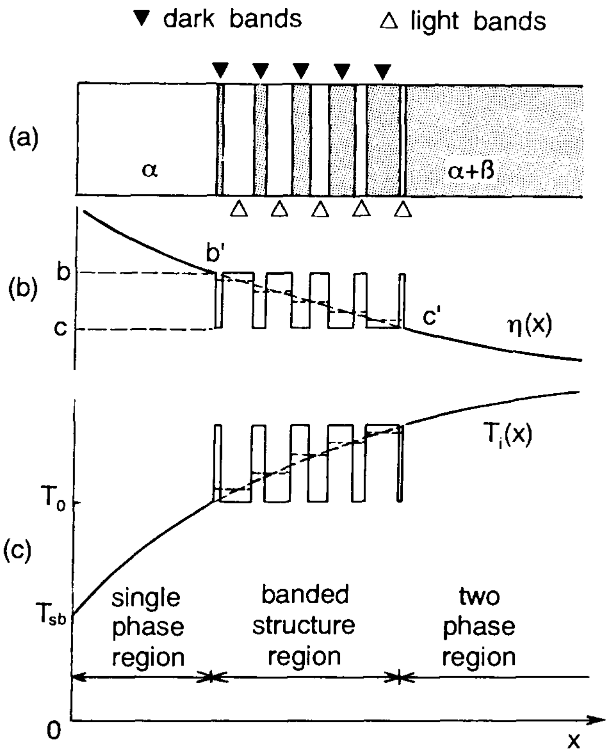

Fig. 9. Diagram showing linkage between the banded structure and incomplete release of the latent heat of fusion and the evolution of the crystallization temperature. (a) An evolutionary structure including a region of the banded structure; (b) the interface response function of the thermal engine efficiency $\eta(x)$, which exhibits an oscillatory curve in the banding region; (c) the interface response function of the crystallization temperature $T_i(x)$.

capacity of an aluminum alloy is taken to be 32 J K^{-1} mol^{-1} and the latent heat of fusion to be 10.47 kJ mol^{-1}, which are for pure aluminum liquid, the 5-K oscillation of the interface temperature should correspond to about 1.5% oscillatory amplitude of the thermal efficiency, $\eta(x)$. The incomplete release effect of the latent heat of fusion plays an adjustment role in the oscillation of the interface temperature.

The formation of the banded structure in the aluminum binary alloys can be understood on the following basis. Because of the existence of a critical activation energy for dispersoid nucleation, the interface response functions of the crystallization temperature $T_i(x)$, Gibbs free energy difference $\Delta G(x)$ and thermal efficiency $\eta(x)$ fluctuate systematically from monotonic changes to oscillations. However, the oscillations correspond to the monotonic functions, which depend on a potential ability of heat extraction by the external cooling environment. This oscillation is probably analogous to the "self-excited oscillation" under the perturbation of a negative resistance.

6. Conclusion

Rapid solidification yields a solid in a nonequilibrium state which is different from the equilibrium state. Therefore, an enthalpy difference ΔH_0^{ne} exists between a rapidly solidified alloy and a fully annealed alloy. The value of ΔH_0^{ne} can be established by a calorimetric evaluation method, and estimations of the value of ΔH_0^{ne} in as-melt spun Al–Si and Al–Mn alloys exhibited clear, non-negligible values compared with the latent heat of fusion of pure aluminum.

The enthalpy difference ΔH_0^{ne} was associated with an excess enthalpy change ΔH_{ex} induced by the nonequilibrium crystallization reaction on rapid solidification; this excess enthalpy change ΔH_{ex}, as a thermal energy, was dissipated at the advancing interface and then stored in the solidified solid as an unreleased part of the latent heat of fusion at the interface. This thermal engine effect, represented by the "thermal engine" efficiency η, reflects the enthalpy aspect of the nonequilibrium crystallization reaction during rapid solidification.

Taking this thermal engine effect and the interface kinetic attachment into account when modeling, a conceptual model of the moving interface was formulated to describe the crystal growth during rapid unidirectional solidification. In this modeling, the crystal–melt interface, as a thermal engine, was treated as a moving boundary between the crystal and melt domains, and it represents a crystallization reaction system, advancing forward and incompletely releasing the latent heat of fusion. The interface response functions of the Gibbs free energy change ΔG, the thermal efficiency η and temperature T_{i} vary systematically with respect to the interface position.

The scheme of the present modeling was approached as a "moving boundary problem (MBP)", which not only describes the advancing position of the interface and temperature distribution in two domains, but also maps the evolution of the interface temperature and latent heat release. This model is different from classical MBP in the joint conditions of temperature and heat flow balance at the two-domain boundary: in the present modeling, the generation of solidification latent heat is constrained by the excess enthalpy effect, and the moving velocity of the boundary is restricted by the interface kinetic attachment. However, these restrictions do not exist in classical MBP. The formation of the banded structure can be understood from the perturbation role of the nucleation behavior in the framework of the present MBP modeling.

References

[1] B.A. Mueller and J.H. Perepezko, Master. Sci. Eng., 98 (1988) 153.
[2] W.J. Boettinger, L. Bendersky and J.G. Early, Metall. Trans., 17A (1986) 781.
[3] W.J. Boettinger, L. Bendersky, R.J. Schaefer and F.S. Biancaniello, Metall. Trans., 19A (1988) 1101.
[4] J.D. Cotton and M.J. Kaufman, Metall. Trans., 22A (1991) 927.
[5] L.A. Bendersky, F.S. Biancaniello, S.D. Ridder and A.J. Shapiro, Mater. Sci. Eng., A134 (1991) 1098.
[6] M. Zimmermann, M. Carrard, M. Gremaud and W. Kurz, Mater. Sci. Eng., 134A (1991) 1278.
[7] M. Gremaud, M. Carrard and W. Kurz, Acta Metall., 38 (1990) 2587; 39 (1991) 1431.
[8] M. Carrard, M. Gremaud, M. Zimmermann and W. Kurz, Acta Metall., 40 (1992) 983.
[9] S.C. Gill and W. Kurz, Acta Metall., 41 (1993) 3563; 43 (1995) 139.
[10] S.R. Coriell and R.F. Sekerka, J. Crystal Growth, 61 (1983) 499.

[11] B. Caroli, C. Caroli and B. Roulet, Acta Metall., 34 (1986) 1867.
[12] W.J. Boettinger and M.J. Aziz, Acta Metall., 37 (1989) 3379.
[13] M.J. Aziz and W.J. Boettinger, Acta Metall.; 42 (1994) 527.
[14] K. Miyazawa and J. Szekely, Metall. Trans., 12A (1981) 1047.
[15] R. Sellyer and W. Loser, Acta Metall., 34 (1986) 831.
[16] G. Trapaga and J. Szekely, Metal. Trans., 22B (1991) 901.
[17] B. Jöisson, Metall. Trans., 22A (1991) 2475.
[18] Y. Zhang, T. Yamane and J. Takahashi, J. Mater. Sci. Lett., 11 (1992) 155.
[19] Y. Zhang, T. Yamane, S. Saji and J. Takahashi, J. Mater. Sci., 28 (1993) 3235; 29 (1994) 2491.
[20] Y. Zhang, T. Yamane, S. Saji and J. Takahashi, Metall. Mater. Trans., 25A (1994) 1102.
[21] A. Kamio, H. Tezuka, T. Sato, Than Trong Long and T. Takahashi, J. Jpn. Inst. Light Metals, 35 (1985) 275.
[22] S.C. Mraw, Rev. Sci. Instrum., 53 (1982) 228.
[23] N. Apaydin and R.W. Smith, Mater. Sci. Eng., 98 (1988) 149.
[24] T. Soma, Y. Funayama and H.M. Kagaya, J. Mater. Sci., 25 (1990) 3917.
[25] Y. Zhang, T. Yamane, S. Saji and J. Takahashi, J. Mater. Sci. Lett., 12 (1993) 1659.
[26] Y. Zhang, Ph.D thesis, Osaka University, 1993 (unpublished).
[27] K. Yu-Zhang, M. Harmelin, A. Quivy, Y. Calvayrac, J. Bigot and R. Portier, Mater. Sci. Eng., 99 (1988) 385.
[28] K.F. Kobayashi, H. Kawaura and P.H. Shingu, E.A. Starke et al. (Eds.), Aluminum Alloys – Physical and Mechanical Properties, Vol. 1, EMAS, Warley, 1986, pp. 247.
[29] M. Harmelin and J. Jiang, Thermochim. Acta, 162 (1990) 453.
[30] J.C. Baker and J.W. Cahn, in Solidification, ASM, Metals Park, OH, 1971, pp. 23.
[31] W. Kurz and D.J. Fisher, Fundamentals of Solidification, Trans Tech Publications, CH-4711, Aedermannsdorf, Switzerland, 1986, pp. 220.
[32] W.J. Boettinger, D. Shechtman, R.J. Schaefer and F.S. Biancaniello, Metall. Trans., 15A (1984) 55.
[33] J. Crank, in R.W. Lewis et al. (Eds.), Numerical Method in Heat Transfer, Wiley and Sons, New York, 1981, pp. 177.
[34] D.G. Beck, S.M. Copley and M. Bass, Metall. Trans., 12A (1981) 1687; 13A (1982) 1879.